Scripta Materialia 162 (2019) 316–320

Contents lists available at ScienceDirect

Scripta Materialia

journal homepage: www.elsevier.com/locate/scriptamat

Unique defect evolution during the plastic deformation of a metal matrix composite

Yanfang Liu [a], Fang Wang [a], Yang Cao [a,*], Jinfeng Nie [a,*], Hao Zhou [a], Huabing Yang [b], Xiangfa Liu [b], Xianghai An [c], Xiaozhou Liao [c], Yonghao Zhao [a], Yuntian Zhu [a,d]

[a] Nano and Heterogeneous Materials Center, School of Materials Science and Engineering, Nanjing University of Science and Technology, Nanjing 210094, China
[b] Key Laboratory for Liquid–Solid Structural Evolution and Processing of Materials, Ministry of Education, Shandong University, Jinan 250061, China
[c] School of Aerospace, Mechanical and Mechatronic Engineering, The University of Sydney, Sydney, NSW 2006, Australia
[d] Department of Materials Science and Engineering, North Carolina State University, Raleigh, NC 27695, USA

ARTICLE INFO

Article history:
Received 28 October 2018
Received in revised form 19 November 2018
Accepted 20 November 2018
Available online xxxx

Keywords:
Dislocation density
Composite
Strain-hardening
Plastic deformation
Microstructure

ABSTRACT

During the plastic deformation of a metal matrix composite (MMC) containing non-deformable particles, high dislocation density and strong back stresses are expected because the particles help with blocking and accumulating dislocations. Here we report that the MMC has lower, instead of higher, dislocation density than the corresponding monolithic matrix material when they are deformed to high plastic strains, because smaller sub-grains in the MMC lowered dislocation generation rate and meanwhile promoted the dislocation interaction and annihilation in the matrix. This unique defect density evolution is a hitherto unknown but important factor affecting the mechanical properties of MMCs.

Composite materials including both multiphase alloys [1–6] and metal matrix composites (MMCs) [7–9] have been continuously developed and widely used in modern industries, thanks to their unique balance of mechanical properties, thermal properties, electrical properties, chemical resistance and tribological properties. For optimal combination of properties, the spatial distribution or dispersion of secondary phases in the form of particles, whiskers or short fibers are carefully engineered [8,10]. Conventionally, the spatial distribution or dispersion of secondary phases are controlled by consolidation processes, such as solidification with ultrasonic stirring and rapid solidification [11], and deformation processes such as rolling and extrusion [8]. However, conventional manufacturing techniques are unable to process composite materials with homogeneous distribution of secondary phases [8,12], due to hardly controllable kinetics of phase transformation [13–15] and/or insufficient strain/energy input [16,17]. In recent years, it has been found that accumulative strain input by plastic deformation is capable of continuously increasing the homogeneity of composite materials [18–22], and consequently improving properties [23].

Due to the presence of the secondary phases, the microstructural evolution of a composite is different from the corresponding monolithic matrix material [24]. Thus, the evolution of mechanical properties of the composites via plastic deformation is consequently very different from the corresponding monolithic matrix material [8,22,24]. For example, the strain-hardening rate of the matrix is much higher than that of the monolithic matrix material, which is mainly attributed to the strong back-stress hardening on top of the common forest dislocation hardening [7]. Back stress is long-range stress caused by the pileup of geometrically necessary dislocations (GNDs) accommodating the strain gradients at the interphase interfaces [25–27]. Back stress becomes significant in a composite material [28], because the high plastic strain gradients near the interphase interfaces in the matrix lead to high densities of GNDs.

The strong back-stress is resulted from the drastic increase in the density of GNDs and leads to the high strain-hardening rate of the MMC at low strain levels. However, the hardening effect of MMCs at high processing strain level has not been explored in-depth. This problem becomes more important, considering the fact that high processing strain is necessary for achieving homogeneous distribution of secondary phase particles in MMCs. In fact, a few work has shown that MMCs have prolonged hardening stage and higher saturation hardness (strength) than the corresponding monolithic matrix materials [29,30], but in-depth explanation of this physical phenomenon is yet to be provided.

In this work, a commercial purity Al (CP-Al) and an Al-5%TiB_2/TiC MMC (Al-3.6TiB_2-1.4TiC) are used as model materials to compare the hardening effects and corresponding microstructural evolution from low to ultrahigh processing strains. TiB_2 and TiC particles are insoluble in Al, thus making them suitable for this study. An Al-5%TiB_2/TiC MMC

* Corresponding authors.
E-mail addresses: y.cao@njust.edu.cn (Y. Cao), niejinfeng@njust.edu.cn (J.F. Nie).

https://doi.org/10.1016/j.scriptamat.2018.11.038
1359-6462/

ingot was fabricated by an in-situ melt reaction method [31]. The ingots of CP-Al and Al-5%TiB_2/TiC MMC were machined into disks and processed by high-pressure torsion (HPT) with a quasi-constrained HPT facility [32,33] at room temperature and under 6 GPa applied pressure. CP-Al disks were HPT processed to 1, 2 and 5 revolutions; Al-5%TiB_2/TiC disks were HPT processed to 1, 2, 5 and 15 revolutions. X-ray diffraction (XRD) measurement was carried out with a Bruker-AXS D8 Advance X-ray diffractometer equipped with Cu-Kα radiation source (λ = 0.1542 nm). Optical microscopy (OM) analysis was conducted with a ZEISS-Axio-Vert-A1 optical microscope. Scanning electron microscopy (SEM) analysis and electron backscatter diffraction (EBSD) were performed with a Quanta 250F scanning electron microscope and a Zeiss Auriga scanning electron microscope, respectively. A TECNAI G2 20 transmission electron microscope (TEM) was used to analyze the microstructures of the materials in detail. Vickers hardness experiment was carried out using a HMV-G 21DT indentation equipment with an applied load of 98.07mN and a dwell time of 15 s for each indent.

The von Mises equivalent shear strain, ε_{eq}, imposed by HPT to the disk samples is estimated as:

$$\varepsilon_{eq} = \frac{2\pi Nr}{h\sqrt{3}} \quad (1)$$

where N is the number of revolutions and r and h are the radius and thickness of the disk, respectively [3,32].

Both as-cast CP-Al and Al-5%TiB_2/TiC MMC ingots have coarse equiaxed Al grains. Fig. 1 is an OM image showing the microstructures at the center of the MMC disk, where the shear strain is theoretically zero. The average grain size of the Al matrix is approximately 40 μm. The TiB_2/TiC particles are mostly agglomerated and distributed along Al grain boundaries (GBs). This kind of microstructure is typical in MMCs made by conventional fabrication methods [8]. Fig. 2(a) shows the morphology and distribution of the TiB_2/TiC particles of light contrast in the as-cast samples. The particles are agglomerated and distributed inhomogeneously, resulting in the mixture of particle-rich regions and particle-lean regions. After HPT processing to 15 revolutions, the ultrahigh shear strain was able to break the agglomeration of TiB_2/TiC particles, resulting in comparatively homogeneous particle distribution as shown in Fig. 2(b).

Comprehensive TEM analysis was conducted to examine the microstructural evolution of the CP-Al and Al-5%TiB_2/TiC MMC samples processed by HPT. TEM results show that as the shear strain increased, dislocation density in Al matrix changed in an undulating manner, but the grain size decreased monotonically. Fig. 3(a) shows typical microstructures of the CP-Al processed to an strain level, $\varepsilon_{eq} = 10.9$. Dislocation structures can be clearly seen inside grains, indicating that dislocation generation still outperformed dynamic recovery. Fig. 3 (b) shows well-developed steady state microstructure in the HPT CP-Al at $\varepsilon_{eq} = 54.1$. The majority of the grains have been refined to the ultrafine-grained regime with well-defined GBs, and dislocation clusters are hardly seen inside grains. In contrast, at the strain level, $\varepsilon_{eq} = 10.9$, the MMC also has a high density of dislocations, and grain sizes are close to 650 nm, as shown by Fig. 3(c). Fig. 3(d) shows the steady state microstructures in the MMC samples, revealing much smaller grain sizes than that in HPT CP-Al.

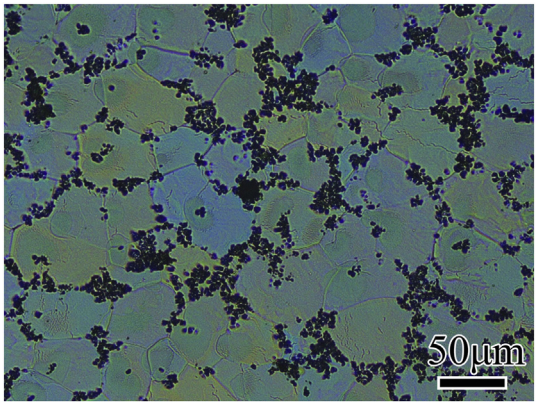

Fig. 1. An optical microscopy image showing the microstructures at the center of the Al-5% TiB_2/TiC disk processed by HPT for 1 revolution.

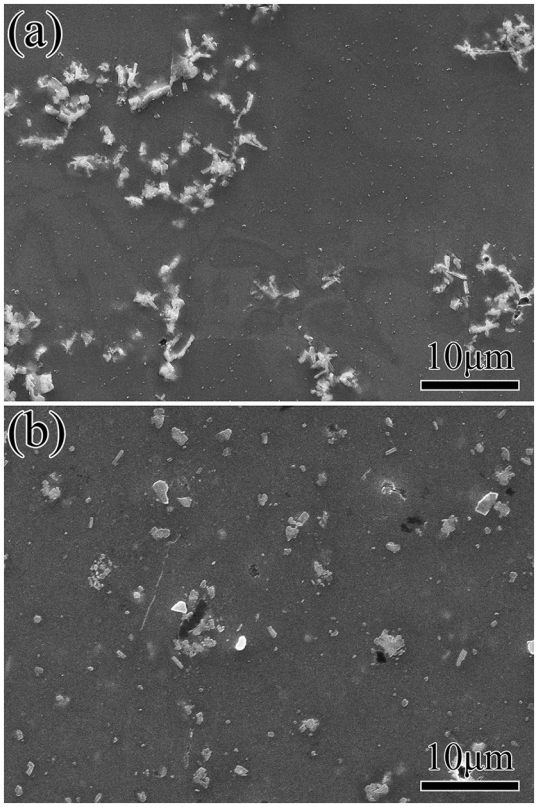

Fig. 2. Scanning electron microscopy images showing typical microstructures of (a) the as-cast Al-5%TiB_2/TiC samples, and (b) the edge of the Al-5%TiB_2/TiC disk, where $\varepsilon_{eq} \approx 162.4$.

The overall hardening produced by accumulative processing strain under HPT shall include (1) strain-hardening due to the increase in dislocation density, (2) GB-strengthening due to grain size reduction, and (3) strengthening by hard particles [24]. Dissolution of secondary phase particles and phase transformation were not detected by XRD or TEM in current experiments. Thereby solid solution strengthening and phase transformation are not considered hereafter. The evolution of dislocation density with increasing shear strain is quantitatively analysed, based on the strain gradient model by Gao et al. [34], by using EBSD data. Assuming that each low angle boundary (misorientation angle <2°) is of twisted nature and contains two perpendicular arrays of screw dislocations for strain accommodation, the density of GNDs can be estimated by the formula [35,36]:

$$\rho_{GND} = \frac{2\theta_{KAM}}{xb} \quad (2)$$

where θ_{KAM} is the kernel average misorientation which can be retrieved directly from EBSD data; x is unit length which is equal to twice the step size used in EBSD acquisition. Binning of 4 × 4 was used for all EBSD acquisition. Step size of 100 nm and 40 nm were chosen for specimens with large (>1 μm) and small (<1 μm) average sub-grain sizes, respectively, for optimised reliability of test [37].

Fig. 4(a) shows the evolution of dislocation density with increasing shear strain. This dislocation density is actually the density of GNDs estimated by formula (2). Although both GNDs and statistically stored

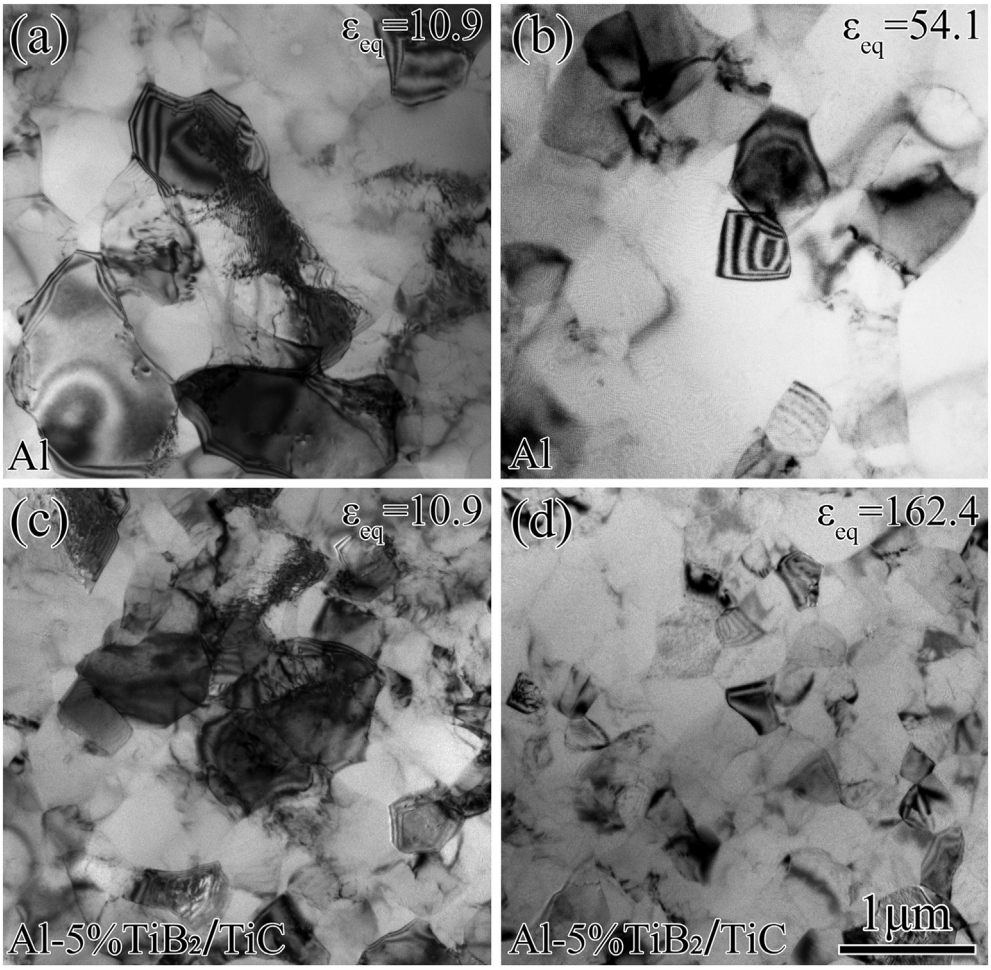

Fig. 3. Transmission electron microscopy images showing detailed microstructures in (a) CP-Al at the strain level $\varepsilon_{eq} \approx 10.9$, (b) CP-Al at the strain level $\varepsilon_{eq} \approx 54.1$, (c) an Al-5%$TiB_2$/TiC MMC at the strain level $\varepsilon_{eq} \approx 10.9$, and (d) an Al-5%$TiB_2$/TiC MMC at the strain level $\varepsilon_{eq} \approx 162.4$.

dislocations (SSDs) contribute to strain-hardening of materials at large strain when dislocations were tangled to form cells and walls, the GNDs contribute to the majority of the flow stress [38,39]. Thus, it is reasonable to inspect the strain-hardening effect by studying the density of GNDs only. At the low strain level (first two data points from left hand side on Fig. 4(a)), the dislocation density in HPT Al-5%TiB_2/TiC MMC was clearly higher than that in the HPT CP-Al. This is because the non-deformable TiB_2/TiC particles cause strong back-stress to build up in the surrounding Al matrix, resulting in additional GNDs and increased strain-hardening rate during plastic flow [7,25]. Interestingly, the dislocation density in HPT CP-Al increased quickly to a peak value of 8.34 $\times 10^{14}$ m^{-2} at $\varepsilon_{eq} = 10.9$. In contrast, the dislocation density in HPT Al-5%TiB_2/TiC MMC at $\varepsilon_{eq} = 10.9$ was unexpectedly only 4.98 $\times 10^{14}$ m^{-2} which was also the peak value for the material. TEM analysis can provide clue in regarding the dislocation density in CP-Al and Al-5% TiB_2/TiC MMC at $\varepsilon_{eq} = 10.9$. By comparing Fig. 3(a) and (c), it can be seen that the average grain sizes in CP-Al and Al-5%TiB_2/TiC MMC are 1000 nm and 650 nm, respectively. Comparatively large grain size of CP-Al allows more space at the grain interior for dislocations than Al-5%TiB_2/TiC MMC. The Al-5%TiB_2/TiC MMC has much smaller grain sizes than CP-Al, and thus much more GBs. GBs are major sinks for dislocations and popular sites for dynamic recovery [40]. In addition, as the grain size reduces to the ultrafine-grained and nano-crystallize regimes, GB activities involving dislocation annihilation become increasingly pronounced [41]. Consequently, an enormous amount of GBs and small grain sizes increased the rate of dynamic recovery, resulting in lower dislocation density in Al-5%TiB_2/TiC MMC than in CP-Al at $\varepsilon_{eq} > 10$.

Fig. 4(b) shows the evolution of average sub-grain size in CP-Al and Al-5%TiB_2/TiC MMC with increasing strain. The average grain sizes were measured from TEM images, and low-angle boundaries and dislocation walls with sharp contrast were recognized as sub-grain boundaries. Therefore, the average grain size measured may be slightly smaller than the actual case. The average grain sizes at $\varepsilon_{eq} < 5$ were too large, and thus were excluded from the plots. Knowing that the initial average grain sizes of CP-Al and Al-5%TiB_2/TiC matrix were 185 μm and 40 μm, respectively; grain refinement by HPT was very effective in both materials. At the strain level higher than 13.5, the curve indicating average grain size vs. equivalent strain for CP-Al suddenly reached a plateau (steady state), indicating that grain size reduction has stopped. In contrast, the grain size reduction in Al-5%TiB_2/TiC matrix continued along a gentle slope until the equivalent strain was increased above ~75.

The most attractive aspect of processing MMCs to high strains is to cause fragmentation/separation and then redistribution of the originally agglomerated secondary phase particles in the matrix [16–18,24]. In the fields of MMCs manufacturing and research, the distribution of secondary phase particles is commonly quantified by the term, contiguity:

$$C_\alpha = \frac{2S_V^{\alpha\alpha}}{2S_V^{\alpha\alpha} + S_V^{\alpha\beta}} \tag{3}$$

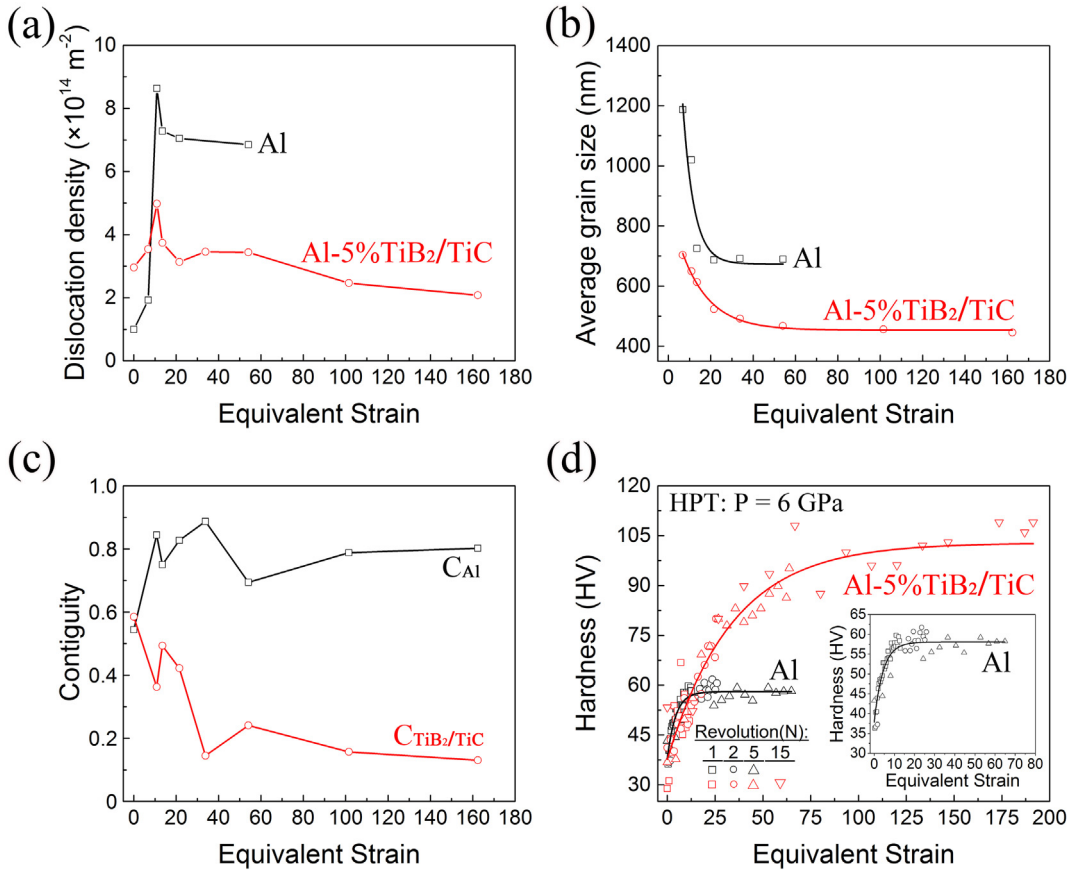

Fig. 4. (a) Dislocation density vs. von Mises equivalent strain, and (b) average grain size vs. von Mises equivalent strain (both GBs and dislocation walls are recognized as sub-grain boundaries), for the HPT processed CP-Al and Al-5%TiB_2/TiC MMC. (c) Contiguity vs. von Mises equivalent strain for the Al matrix and TiB_2/TiC particles in HPT Al-5%TiB_2/TiC MMC. (d) Hardness vs. von Mises equivalent strain for the HPT processed CP-Al and Al-5%TiB_2/TiC MMC.

$$C_\beta = \frac{2S_V^{\beta\beta}}{2S_V^{\beta\beta} + S_V^{\alpha\beta}} \tag{4}$$

where

C_α and C_β are contiguities of matrix and secondary phases, respectively. $S_V^{\alpha\alpha}$ is the total GB area of matrix grains per unit volume, $S_V^{\beta\beta}$ is the total GB area of secondary phase per unit volume, and $S_V^{\alpha\beta}$ is the total surface area of interphase interfaces per unit volume. According to formulae (3) and (4), the higher the homogeneity of the microstructure, C_α is closer to 1 and C_β is closer to 0. Although, C_α and C_β describe the spatial homogeneity of MMCs, they are commonly derived based on two-dimensional micrographs such as EBSD data [8,42]. Similar 2D approach was carried out in this work, and the evolution of contiguities of matrix and secondary phase particles with increasing shear strain was depicted in Fig. 4(c). At the center of the HPT samples, where the shear strain is theoretically zero and the particles distribution is nearly identical to the as-casted samples. At this strain level, the Al matrix grains were very large (~40 μm in average), so the total GB areas were comparatively small. TiB_2/TiC particles agglomerated along GBs of Al grains as exemplified in Fig. 1. Consequently, the value of $S_V^{\alpha\alpha}$ was at the minimum, and the value of $S_V^{\beta\beta}$ was at the maximum. Then, the contiguities of Al matrix and TiB_2/TiC particles were estimated to be 0.544 and 0.585, respectively. As the shear strain increased to 10.9, the contiguity of Al matrix (C_{Al}) was quickly increased to 0.844, and the contiguity of TiB_2/TiC particles ($C_{TiB2/TiC}$) was decreased to 0.363. The increase in C_{Al} was mainly due to the significant grain refinement (increase in GB areas). The majority of TiB_2/TiC particles had not been separated apart; therefore, the drop in $C_{TiB2/TiC}$ was moderate. As the shear strain increased further, the value of C_{Al} varied in a range close to 0.8, and eventually leveled off and reached a value of 0.802 at the strain of ~162. Interestingly, the peak value of 0.887 of C_{Al} was at $\varepsilon_{eq} = 33.8$. At this strain level, the average grain size of Al matrix was 492 nm (Fig. 4(b)), which was very close to the steady state grain size of 446 nm. Meanwhile, there was still a considerable amount of TiB_2/TiC particles which had not been separated apart. Therefore, the term $S_V^{\alpha\alpha}$ for Al matrix was close to the maximum, but $S_V^{\alpha\beta}$ was yet to reach the maximum. Eventually, when the microstructural evolution has reached the steady state, $S_V^{\alpha\beta}$ could reach the maximum, resulting in a moderate drop of the C_{Al}. The value of $C_{TiB2/TiC}$ reflects the homogeneity of distribution of TiB_2/TiC particles. According to Fig. 4(c), the value of $C_{TiB2/TiC}$ dropped at a comparatively fast rate until ε_{eq} = ~40. With further increase in shear strain, value of $C_{TiB2/TiC}$ decreased with undulations and eventually reached a minimum. This was because in the strain range of 0–40, the majority of the work was consumed by grain refinement processes where dislocation activities were dominant. Although the particles could be broken apart by interactions with dislocations [24]; without sufficient GB activities such as GB sliding and grain rotation [43], the particles could not be separated much further. During subsequent deformation process, the particles could collide back together and thus shift the value of $C_{TiB2/TiC}$ up and down with increasing strain.

Hardness were measured to study the relationship between hardness (strength) and processing strain. As shown in Fig. 4(d), the hardness of CP-Al quickly reached the saturation value of ~58 Hv when the shear strain was increased above ~10. This is consistent with the literature report [44] that $\varepsilon_{eq} > 11$ is sufficient to develop the steady-state hardness in CP-Al. In contrast, the hardening continued in HPT Al-5% TiB_2/TiC MMC until the equivalent strain was increased above ~75, revealing a significantly prolonged hardening stage and corresponding

extension of microstructural evolution in the composite material. The Al-5%TiB_2/TiC MMC has much higher saturation hardness (~102 Hv) than the CP-Al, mainly due to smaller grain size and reinforcement particles. The hardness-strain data were fitted by black and red curves for CP-Al and Al-5%TiB_2/TiC MMC, respectively. Close examination of the fitting curves reveals that the curve for CP-Al is much steeper than the curve for Al-5%TiB_2/TiC MMC at the strain levels below ~10, indicating that the hardening rate of CP-Al at low strain is higher than that of the Al-5%TiB_2/TiC MMC. The two curves intersect at $\varepsilon_{eq} \approx 11.9$, because the hardening effect in CP-Al quickly diminished after the intersection strain while the hardening in Al-5%TiB_2/TiC MMC was still ongoing with increasing strain until $\varepsilon_{eq} \approx 75$. It is worth to mention that despite the dislocation density spikes in Fig. 4(a), the measured hardness in Fig. 4(d) did not show corresponding "spikes" at the strain for both materials. This is because the hardness of HPT materials are affected by several factors including dislocation density, grain size, hard particles, interfacial bonding strength and even local microstructural heterogeneity [3,24], thus making the single effect of a dislocation density spike less distinguishable on the fitting curves in Fig. 4(d).

It has been widely observed in early study that composite materials have very high strain-hardening rate at the initial stage of plastic flow [7,8,12,22,24,28]. However, study by Lloyd [45] has revealed that the high strain-hardening rate in MMCs could not be sustained even in coarse grained materials due to the activation of stress relaxation processes including: (1) dislocation rearrangements; (2) interfacial sliding; (3) diffusion; and (4) cavitation (particle cracking, interfacial debonding, void formation in matrix). According to literatures [46,47] and current results, fast grain refinement to the ultrafine-grained regime can further boost these stress relaxation mechanisms due to active GB activities, thus postponing the overall hardening effect in the Al-5%TiB_2/TiC MMC processed by HPT.

In conclusion, the hardness/strength evolution of an Al-5%TiB_2/TiC MMC with respect to increasing strain was a combined effect of strain-hardening, GB-strengthening, and strengthening by hard particles. The presence of hard secondary phase particles accelerated dislocation generation and accumulation until the average sub-grain size was reduced below 1000 nm. Then, the small grain size began to suppress dislocation slip, thus lowered the strain-hardening effect. Both dislocation slip and GB activities contributed to the separation and redistribution of secondary phase particles, but GB activities took a major and long lasting part. The reduced steady state grain size and homogeneously distributed hard particles significantly increased the steady state hardness (strength) of the MMC in comparison to CP-Al. The suppression on strain-hardening due to fast grain size reduction at medium to high strain level, postponed the overall hardening effect in the Al-5%TiB_2/TiC MMC. The postponed overall hardening effect, the significantly increased steady state hardness and the additional strain required for redistributing secondary phase particles, together lead to the significantly prolonged microstructural evolution of the Al-5%TiB_2/TiC MMC under accumulative processing strain.

Acknowledgements

This work is supported by the National Key R&D Program of China (2017YFA0204403), National Natural Science Foundation of China (Grant No. 51601094 (Y.C.), Grant No. 51501092 (J.F.N.) and Grant No. 51731007 (X.F.L.)), Australian Research Council (DP150101121) and U.S. Army Research Office (W911 NF-17-1-0350). The authors are thankful for the technical support from Jiangsu Key Laboratory of Advanced Micro&Nano Materials and Technology, and the Materials Characterization Facility of Nanjing University of Science and Technology.

References

[1] J.O. Nilsson, Mater. Sci. Technol. 8 (8) (1992) 685–700.
[2] J.H. Chen, E. Costan, M.A. van Huis, Q. Xu, H.W. Zandbergen, Science 312 (5772) (2006) 416–419.
[3] Y. Cao, Y.B. Wang, R.B. Figueiredo, L. Chang, X.Z. Liao, M. Kawasaki, W.L. Zheng, S.P. Ringer, T.G. Langdon, Y.T. Zhu, Acta Mater. 59 (10) (2011) 3903–3914.
[4] S.J. Zheng, I.J. Beyerlein, J.S. Carpenter, K.W. Kang, J. Wang, W.Z. Han, N.A. Mara, Nat. Commun. 4 (2013) 1696.
[5] S.J. Zheng, J. Wang, J.S. Carpenter, W.M. Mook, P.O. Dickerson, N.A. Mara, I.J. Beyerlein, Acta Mater. 79 (2014) 282–291.
[6] S.H. Jiang, H. Wang, Y. Wu, X.J. Liu, H.H. Chen, M.J. Yao, B. Gault, D. Ponge, D. Raabe, A. Hirata, M.W. Chen, Y.D. Wang, Z.P. Lu, Nature 544 (7651) (2017) (460–+).
[7] I. Sinclair, P.J. Gregson, Mater. Sci. Technol. 13 (9) (1997) 709–726.
[8] L.J. Huang, L. Geng, H.X. Peng, Prog. Mater. Sci. 71 (2015) 93–168.
[9] Y. Cao, L.C. Zhang, Y. Zhang, Mater. Sci. Eng. A-Struct. Mater. Prop. Microstruct. Process. 658 (2016) 321–325.
[10] C.M. Allen, K.A.Q. O'Reilly, B. Cantor, P.V. Evans, Prog. Mater. Sci. 43 (2) (1998) 89–170.
[11] Y. Yang, J. Lan, X. Li, Mater. Sci. Eng. A 380 (1) (2004) 378–383.
[12] J.S. Moya, S. Lopez-Esteban, C. Pecharromán, Prog. Mater. Sci. 52 (7) (2007) 1017–1090.
[13] H.-W. Yen, P.-Y. Chen, C.-Y. Huang, J.-R. Yang, Acta Mater. 59 (16) (2011) 6264–6274.
[14] J.H. Li, X.D. Wang, T.H. Ludwig, Y. Tsunekawa, L. Arnberg, J.Z. Jiang, P. Schumacher, Acta Mater. 84 (2015) 153–163.
[15] E. Alshmri, H.V. Atkinson, S.V. Hainsworth, C. Haidon, S.D.A. Lawes, Wear 313 (1–2) (2014) 106–116.
[16] A.P. Zhilyaev, J.M. García-Infanta, F. Carreño, T.G. Langdon, O.A. Ruano, Scr. Mater. 57 (8) (2007) 763–765.
[17] Y. Cao, M. Kawasaki, Y.B. Wang, S.N. Alhajeri, X.Z. Liao, W.L. Zheng, S.P. Ringer, Y.T. Zhu, T.G. Langdon, J. Mater. Sci. 45 (17) (2010) 4545–4553.
[18] I. Sabirov, O. Kolednik, R.Z. Valiev, R. Pippan, Acta Mater. 53 (18) (2005) 4919–4930.
[19] A. Bachmaier, A. Hohenwarter, R. Pippan, Scr. Mater. 61 (11) (2009) 1016–1019.
[20] Y. Cao, Y.B. Wang, S.N. Alhajeri, X.Z. Liao, W.L. Zheng, S.P. Ringer, T.G. Langdon, Y.T. Zhu, J. Mater. Sci. 45 (3) (2010) 765–770.
[21] K. Edalati, S. Toh, H. Iwaoka, Z. Horita, Acta Mater. 60 (9) (2012) 3885–3893.
[22] C.L. Li, Q.S. Mei, J.Y. Li, F. Chen, Y. Ma, X.M. Mei, Scr. Mater. 153 (2018) 27–30.
[23] A. Ma, K. Suzuki, Y. Nishida, N. Saito, I. Shigematsu, M. Takagi, H. Iwata, A. Watazu, T. Imura, Acta Mater. 53 (1) (2005) 211–220.
[24] Y. Cao, S. Ni, X. Liao, M. Song, Y. Zhu, Mater. Sci. Eng. R. Rep. 133 (2018) 1–59.
[25] X. Wu, Y. Zhu, Mater. Res. Lett. 5 (8) (2017) 527–532.
[26] X. Liu, F. Yuan, Y. Zhu, X. Wu, Scr. Mater. 150 (2018) 57–60.
[27] M. Yang, Y. Pan, F. Yuan, Y. Zhu, X. Wu, Mater. Res. Lett. 4 (3) (2016) 145–151.
[28] R. Xu, G. Fan, Z. Tan, G. Ji, C. Chen, B. Beausir, D.-B. Xiong, Q. Guo, C. Guo, Z. Li, D. Zhang, Mater. Res. Lett. 6 (2) (2018) 113–120.
[29] T. Nizolek, I.J. Beyerlein, N.A. Mara, J.T. Avallone, T.M. Pollock, Appl. Phys. Lett. 108 (5) (2016), 051903.
[30] Y.Z. Tian, S.D. Wu, Z.F. Zhang, R.B. Figueiredo, N. Gao, T.G. Langdon, Acta Mater. 59 (7) (2011) 2783–2796.
[31] J. Nie, D. Li, E. Wang, X. Liu, J. Alloys Compd. 613 (2014) 407–412.
[32] A.P. Zhilyaev, T.G. Langdon, Prog. Mater. Sci. 53 (6) (2008) 893–979.
[33] X.H. An, Q.Y. Lin, G. Sha, M.X. Huang, S.P. Ringer, Y.T. Zhu, X.Z. Liao, Acta Mater. 109 (2016) 300–313.
[34] H. Gao, Y. Huang, W.D. Nix, J.W. Hutchinson, J. Mech. Phys. Solids 47 (6) (1999) 1239–1263.
[35] M. Calcagnotto, D. Ponge, E. Demir, D. Raabe, Mater. Sci. Eng. A 527 (10) (2010) 2738–2746.
[36] P.J. Konijnenberg, S. Zaefferer, D. Raabe, Acta Mater. 99 (2015) 402–414.
[37] J. Jiang, T.B. Britton, A.J. Wilkinson, Ultramicroscopy 125 (2013) 1–9.
[38] N. Hansen, X. Huang, Acta Mater. 46 (5) (1998) 1827–1836.
[39] L.P. Kubin, A. Mortensen, Scr. Mater. 48 (2) (2003) 119–125.
[40] X. Li, Y. Wei, W. Yang, H. Gao, Proc. Natl. Acad. Sci. 106 (38) (2009) 16108–16113.
[41] L.H. Wang, X.D. Han, P. Liu, Y.H. Yue, Z. Zhang, E. Ma, Phys. Rev. Lett. 105 (13) (2010) 135501.
[42] B. Roebuck, K.P. Mingard, H. Jones, E.G. Bennett, Int. J. Refract. Met. Hard Mater. 62 (2017) 161–169.
[43] Z. Shan, E.A. Stach, J.M.K. Wiezorek, J.A. Knapp, D.M. Follstaedt, S.X. Mao, Science 305 (5684) (2004) 654–657.
[44] A.P. Zhilyaev, K. Oh-Ishi, T.G. Langdon, T.R. McNelley, Mater. Sci. Eng. A 410–411 (0) (2005) 277–280.
[45] D.J. Lloyd, Acta Metall. Mater. 39 (1) (1991) 59–71.
[46] K. Oh-Ishi, K. Edalati, H.S. Kim, K. Hono, Z. Horita, Acta Mater. 61 (9) (2013) 3482–3489.
[47] T.H. Fang, W.L. Li, N.R. Tao, K. Lu, Science 331 (6024) (2011) 1587–1590.